



Title	MnO nanocrystals incorporated in a N-containing carbon matrix for Li ion battery anodes
Author(s)	Zhu, Chunyu; Han, Cheng-gong; Saito, Genki; Akiyama, Tomohiro
Citation	RSC advances, 6(36), 30445-30453 <a href="https://doi.org/10.1039/c6ra00571c">https://doi.org/10.1039/c6ra00571c</a>
Issue Date	2016-03-16
Doc URL	<a href="http://hdl.handle.net/2115/64713">http://hdl.handle.net/2115/64713</a>
Type	article (author version)
File Information	manu.pdf



[Instructions for use](#)

# **MnO nanocrystals incorporated in N-containing carbon matrix for Li ion battery anodes**

Chunyu Zhu <sup>a\*</sup>, Cheng-gong Han <sup>a</sup>, Genki Saito <sup>a</sup>, Tomohiro Akiyama <sup>a</sup>

<sup>a</sup>Center for Advanced Research of Energy & Materials, Hokkaido University, Sapporo  
060-8628, Japan

\*Corresponding author: Tel.: +81-11-706-6842; Fax: +81-11-726-0731.

E-mail address: chunyu6zhu@gmail.com or chunyu6zhu@eng.hokudai.ac.jp (Chunyu Zhu)

## **Abstract**

In this study, MnO nanocrystals as-incorporated in N-containing carbon matrix were fabricated by a facile thermal decomposition of manganese nitrate-glycine gels. MnO/C composites with different carbon contents were prepared by controlling the initial ratio of manganese to glycine. The composition, phase structure and morphology of the composites were characterized by X-ray diffraction, X-ray photoelectron spectroscopy, Raman spectroscopy, scanning and transmission electron microscopy, and thermogravimetric analysis. The results indicated that MnO nanocrystals were uniformly embedded in the N-doped carbon matrix. The carbon matrix could effectively enhance the electrical conductivity of MnO and alleviate the strain arising from the discharge/charge cycling. The composite materials exhibited high discharge/charge capacities, superior cycling performance, and excellent rate capability. A high reversible capacity of 556 mAh g<sup>-1</sup> was obtained after 110 cycles of discharge and charge at a current rate of 0.5 A g<sup>-1</sup>. Even at a high current rate of 3 A g<sup>-1</sup>, the sample still delivered a capacity of around 286 mAh g<sup>-1</sup>. The easy production and superior electrochemical properties enables the composites to be promising candidates as an anode alternative for high-performance lithium-ion batteries.

**Keywords:** manganese oxide, lithium ion battery, anode material, composite, carbon

## 1. Introduction

Lithium ion batteries (LIBs) have been considered as one of the most promising power sources for application in mobile electronic devices and electric vehicles (EVs) because of their high energy density and long lifespan.<sup>1, 2</sup> In pursuing next generation, high-capacity LIBs, transition metal oxides ( $\text{MO}_x$ ,  $M = \text{Fe}, \text{Mn}, \text{Co}, \text{Ni}, \text{Cu}$ , etc.) have been investigated as improved negative materials because of their high theoretical capacities ( $>700 \text{ mA h g}^{-1}$ ) as compared with commercial graphite (theoretical capacity of  $372 \text{ mAh g}^{-1}$ ).<sup>3, 4</sup> Among the various transition metal oxides investigated for LIBs, manganese monoxide (MnO) is an attractive anode material due to its high theoretical capacity of  $755.6 \text{ mAh g}^{-1}$ , low plateau voltage, low potential hysteresis ( $< 0.8 \text{ V}$ ), low cost, environmental benignity, and abundance. However, poor cycling performance and low rate capability have hindered the practical application of MnO in LIBs. This originates from the poor electrical conductivity and large volume expansion/shrinkage during the Li insertion/extraction processes.<sup>5-7</sup> Nanostructuring of the active material, with a shortened transport path for  $\text{Li}^+$ , is an effective method to solve the aforementioned problems. However, the risk of side reactions increases with the surface area, leading to a poor electrochemical cycling performance.<sup>8, 9</sup> Moreover, nanomaterials easily aggregate due to their high activities, and exhibit difficulties in the electrode coating process, which make the nanomaterials fail to meet the demand for large-scale applications. Compositing of nanosized oxide active materials with carbon materials into micron-sized structures with a limited surface area can effectively enhance the cycling performance. The carbon matrix acts as both a volume buffer and a conductive network to accommodate the internal stress and increase the electrical conductivity.<sup>10-13</sup> However, fabricating MnO/C anodes with controlled carbon contents by a facile and scalable method remains a great challenge. In this study, we present a facile method that directly produces MnO nanocrystals as-incorporated in carbon matrix. The carbon content in the MnO/C composite was controlled to determine the optimal composites with superior cycling performance and excellent rate capability for a LIB anode.

## 2. Experimental section

**2.1 Synthesis of MnO/C composite:** In the experiment, firstly manganese nitrate ( $\text{Mn}(\text{NO}_3)_2$ , 5 mmol) and glycine ( $\text{NH}_2\text{CH}_2\text{COOH}$ ) in molar ratios of 1:n ( $n = 2.5, 3, 4, 5, 6$ ) were dissolved in distilled water to form homogenous solutions. Next, the solutions were evaporated on a hot plate with magnetic stirring to form dried gels. The gels were heated at 500 °C for 30 min under Ar flow to decompose the nitrate and organic material. Subsequently, the pyrolyzed samples were milled using mortar-pestle for 10 min. Finally, the samples were heated at 700 °C for 1 h under Ar flow to obtain stable composites of MnO/C. The samples were labeled as n2.5, n3, n4, n5, and n6. As a comparison, a sample of glycine-pyrolyzed carbon (ng, from only glycine) was also prepared in the same manner by excluding the addition of manganese nitrate.

**2.2 Material characterization:** The synthesized samples were characterized by X-ray diffraction (XRD, Rigaku Miniflex,  $\text{CuK}\alpha$ ), transmission electron microscopy (TEM, 200 kV, JEM-2010F), and scanning electron microscopy (SEM, JEOL, JSM-7400F) combined with X-ray energy dispersive spectrometry (EDS) to analyze their crystalline structure, morphology and elemental composition, respectively. A thermogravimetric (TG, Mettler Toledo) analyzer combined with a mass spectrometer (MS) was used to determine the carbon content and the combustion gases of the composites. Raman spectra of the samples were acquired from a RENISHAW Raman spectrometer using an excitation wavelength of 532 nm. Surface functional groups and bonding characterization of the samples were performed on X-ray photoelectron spectroscopy (XPS, JEOL, JPS-9200) system using  $\text{MgK}\alpha$  X-ray source.

**2.3 Electrochemical measurement:** A two-electrode union-joint cell (a modified Swagelok cell) was used for the electrochemical test.<sup>14</sup> The cell was assembled in an Ar-filled glove-box. The working electrode consisted of the active material, acetylene black conductive carbon, and polyvinylidene fluoride (PVDF) binder in a 80:10:10 weight ratio. The mass load of the working electrode is around 2-3 mg. A lithium disk was used as the reference and counter electrode, and a 1 M solution of  $\text{LiPF}_6$

dissolved in a 50:50 (v/v) mixture of ethylene carbonate (EC) and dimethyl carbonate (DMC) was used as the electrolyte. Galvanostatic discharge/charge measurement was performed using an Arbin battery tester in a potential range of 3.0 and 0.01 V versus  $\text{Li/Li}^+$  at a constant temperature of 25 °C.

### 3. Results and discussion

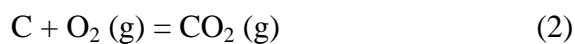
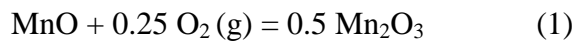
#### 3.1 Materials characterization

The phase composition of the samples was analyzed by XRD, as shown in Figure 1(a). For samples from n2.5 to n5, clear diffraction peaks present, which can be indexed to a single phase of MnO (JCPDS no. 07-0230). The XRD peaks exhibit decreased intensity with increasing values of n, and the XRD pattern of sample n6 is almost amorphous. It is noted that with the increasing amounts of glycine the composite materials contain larger amount of carbon. The sample ng, as-derived from pyrolyzed glycine, indicates the typical peaks of graphite carbon with amorphous feature, illustrating a broadened peak at around 20–30 degree.

Figure 1(b) shows the Raman spectra of the samples. A weak peak at about 650  $\text{cm}^{-1}$  was observed in the spectra for samples from n2.5 to n5. This peak is consistent with the reported  $A_{1g}$  active mode of  $\text{Mn}_3\text{O}_4$ . Here, the typical peak of  $\text{Mn}_3\text{O}_4$ , rather than MnO, is observed although the oxide phase was confirmed to be MnO by XRD analysis. This is attributed to that MnO is easily transformed into  $\text{Mn}_3\text{O}_4$  by the local heating effect and photochemically induced transformations, occurring when the beam intensity is more than 1.1 MW during the Raman measurements.<sup>15, 16</sup> The samples show a decreasing tendency of the MnO peak intensity with increasing carbon content, and the MnO peak is almost negligible for sample n6. Two strong peaks at about 1355 and 1570  $\text{cm}^{-1}$  are observed for all samples. This is assigned to the D-band and G-band of carbon, indicative of the disordered carbon and ordered graphitic carbon, respectively. The ratios of the intensities of the D-band to G-band,  $I_D/I_G$ , are higher than 1 for the MnO/C composite materials which is much larger than the fully graphitized carbon, indicating a highly defective state of the carbon matrix. With the increasing carbon content,  $I_D/I_G$  decreases and is slightly less than 1 for sample ng. This defective structure of carbon may be favorable for increasing the lithium storage capacity. In fact, the carbon matrix of the composite materials is an N-containing carbon, which is confirmed by the following XPS, MS, and EDS measurements.

XPS was conducted to investigate the functional groups of the materials, as shown in Figure 2. The XPS survey spectra (Figure 2 (a)) of the MnO/C composites from n2.5 to n6 exhibit five peaks at 286.7, 399.5, 530.5, 641.7, and 653.6 eV, corresponding to C 1s, N 1s, O 1s, Mn 2p<sub>3/2</sub>, and Mn 2p<sub>1/2</sub>, respectively. In contrast, the spectrum of sample ng shows similar peaks corresponding to C 1s, N 1s, and O 1s, excluding the peaks corresponding to manganese. These results confirm that the carbon matrix is N-doped. A rough quantitative analysis of these samples indicates a decreasing tendency of the atomic percentage of Mn and an increasing tendency for C in the samples from n2.5 to ng. The N 1s and C 1s spectra were further carefully observed as presented in Figure 2 (b, c), showing the results for sample n4 as an example. The XPS spectrum of N 1s can be divided into three component peaks, which can be assigned to the pyridinic N (~398.5 eV), pyrrolic N (~399.7 eV), and quaternary N (~400.5 eV), respectively. The C 1s peaks can be resolved into three components centered at 284.8, 286.2, and 288.2 eV, which can be ascribed to graphitic sp<sup>2</sup> C, N-sp<sup>2</sup> C, and N-sp<sup>3</sup> C, respectively.<sup>17, 18</sup> N-doping enhances the electronic conductivity of carbon-based materials, which therefore improves the electrochemical performance. Furthermore, this type of N-doped carbon possesses more Li storage sites than graphitic carbon, increasing its capacity as stored in carbon.<sup>19-22</sup>

The carbon contents of the samples were determined by TG analysis. All samples were heated to 800 °C at a temperature ramp of 10 °C min<sup>-1</sup> under an air flow. Figure 3 shows the TG profiles. The composites, containing MnO and carbon, were oxidized to Mn<sub>2</sub>O<sub>3</sub> and CO<sub>2</sub> gas based on the following reactions:



Assuming that the ratio of carbon in the composite is  $x$  ( $0 < x < 1$ ), then the ratio for MnO is  $(1-x)$ . Therefore, we can obtain the following equation:



$$Y = \frac{0.5 \times 157.87 \times (1-x)}{70.94} \quad (3)$$

Here, Y ( $0 < Y < 1$ ) is the weight ratio after oxidation, i.e. the weight ratio read from the TG scale at 800 °C; 157.87 is the molecular weight for  $\text{Mn}_2\text{O}_3$  and 70.94 is the molecular weight for MnO. Therefore, the carbon ratios are calculated to be 19.63%, 27.99%, 49.49%, 56.03%, and 62.83% for the samples n2.5, n3, n4, n5, and n6, respectively.

The air-combusted gases during TG analysis were also analyzed by a mass spectrometer. The results indicate the release of NO and  $\text{CO}_2$  gases as shown in Figure S1 (Electronic Supplementary Information, SEI).  $\text{CO}_2$  was released due to the combustion of carbon. NO was also detected, confirming that the carbon contains nitrogenous element. This is consistent with the Raman and XPS analysis.

The morphology of the samples was observed using SEM. Figure 4 shows the typical SEM images of the samples at different magnifications. Porous agglomerates in the scale of several microns to several tens of microns are observed for samples n2.5 and n3. Samples n4, n5, n6, and ng exhibit irregular bulky shapes ranging from several microns to several tens of microns in size. The surface morphology greatly differs between these samples. Samples n4 and n5 exhibit many cubic crystals with size ranging from 200 to 500 nm which are embedded in the bulk carbon matrix. We know that MnO has a halite cubic crystal structure, and these cubic crystals were confirmed to be MnO as detected by the EDS elemental mapping. The EDS results illustrate the enrichment of oxygen and manganese elements in the cubic shape. Occasionally, some cubic crystals are also observed on the surface of the smooth bulk composite for sample n6. As a comparison, sample ng shows irregular bulky shapes with a smooth surface morphology. The microstructure of the composites was further investigated via TEM analysis. Figure 5 shows the typical bright-field TEM image and high-resolution TEM image for sample n4. The selected area diffraction pattern is also presented which can be indexed to a single phase of MnO. It is observed that

MnO nanocrystals of several nanometers are incorporated in the amorphous carbon matrix. It is concluded that samples n4 and n5 contain cubic crystals larger than 100 nm and nanocrystals of several nanometers, all of which are incorporated into the carbon matrix. To further confirm this, samples n4 and n5 were heat-treated under air at 400 °C for 2 h. Under this condition, the MnO/C composites were oxidized to form Mn<sub>2</sub>O<sub>3</sub> as confirmed by XRD analysis in Figure S2 (SEI). The SEM image and EDS spectra of the sample after oxidation are also presented. The sample contains large cubic crystals of about 200–500 nm in size, which are surrounded by nanoparticles of about 20 nm. The cubic crystals originate from the MnO cubic crystals in the composites, which almost maintain their shape after oxidation. The ~20 nm nanoparticles derive from the MnO nanoparticles of several nanometers in the composite. It is noted that the MnO crystals with different sizes exhibit crystal growth to form Mn<sub>2</sub>O<sub>3</sub> due to the removal of the carbon matrix and sintering under air.

### 3.2 Electrochemical performance

The electrochemical properties of the synthesized samples were firstly characterized by galvanostatic discharge and charge cycling. Figure 6 presents the cycling performance of the obtained samples at a current density of 0.5 A g<sup>-1</sup> and their corresponding Coulombic efficiency for lithium extraction to insertion. In this work, the specific capacities were calculated based on the weight of the entire composites. Table 1 summarizes the cycling performance of the samples at a current density of 0.5 A g<sup>-1</sup>, including the first discharge and charge capacities, the initial Coulombic efficiencies, the capacities at 110th cycle, and the capacity retention after 110 cycles of the electrodes. Obviously, sample n4 demonstrates the best cycling performance. This sample exhibits the highest initial Coulombic efficiency of 67.12% and the highest capacity retention of 96.16% after 110 cycles with a charge capacity of 556.03 mAh g<sup>-1</sup> at the 110th cycle. As shown in Figure 6 (b), samples n4 and n5 display the highest Coulombic efficiency during cycling. These samples demonstrate high values

of Coulombic efficiency larger than 97% from the second cycle and the values stabilize at around 99.7% with increasing the cycling numbers.

Figure 7 shows the discharge and charge curves cycled at  $0.5 \text{ A g}^{-1}$  within a cutoff voltage window of 0.01-3.0 V. During the initial discharge process, a continuous and slow voltage decrease is observed for the MnO/C composite samples from about 0.6 V to 0.01 V, which comprises most of the capacity. This behavior is related to the reduction of  $\text{Mn}^{2+}$  to  $\text{Mn}^0$ , the lithium insertion into carbon, and the irreversible part of capacity caused by the formation of solid electrolyte interface (SEI) and decomposition of electrolyte. For samples n2.5 and n3 with lower carbon contents, voltage plateaus are observed at about 0.3 V, which represents the reduction of  $\text{Mn}^{2+}$  to  $\text{Mn}^0$ . However, with the increasing amount of carbon in samples n4, n5, and n6, the plateaus are indistinct. This is due to the combination of the lithium storage in oxide and carbon phases, and the formation of SEI and decomposition of electrolyte. For the carbon sample derived from the decomposition of glycine, a continuous and slow voltage decrease is observed from 0.3 V to 0.01 V. For the opposite charge process, slopes are observed between 0.9 V to 2.0 V, which are associated with the oxidation of  $\text{Mn}^0$  to  $\text{Mn}^{2+}$  and the lithium extraction from carbon materials. These are the typical voltage trends for MnO or MnO/C electrodes.<sup>15, 23, 24</sup> The first discharge capacities of the composite samples are summarized in Table 1, and all are larger than the theoretical capacity of MnO. The initial Coulombic efficiency for these samples range from 49.24% to 67.12%, indicating a large capacity loss in the first cycle. This is primarily ascribed to the formation of a SEI film on the surface of the electrode and the decomposition of electrolyte, similar to previous reports on LIB anodes.<sup>25, 26</sup> From the second cycle, the discharge and charge profiles shift to higher potentials, which might result from increased polarization and the irreversible formation of Mn and  $\text{Li}_2\text{O}$ . The deterioration of the electrochemical performance is least significant for sample n4, which exhibits the smallest increase of polarization upon cycling.

The lithium insertion and extraction behavior were further evaluated by CV analysis. Figure 8 shows the CV curves of the MnO/C composite electrodes and the glycine-derived carbon electrode at a scan rate of  $0.1 \text{ mV s}^{-1}$ . The first cathodic peaks

of the electrodes are quite different for the samples with different amount carbon matrix, which is ascribed to the different environment as the MnO particles inside the carbon matrix. For samples n2.5 and n3 with lower carbon contents, the first CV curves present two obvious cathodic peaks at around 0.15–0.2 and 0.01–0.03 V. For samples n4, n5, and n6 with higher carbon contents, the first CV curves show a broadened peak at around 0.4 V and a sharp peak at around 0.01 V. The former peaks correspond to the reduction of  $\text{Mn}^{2+}$  to metallic  $\text{Mn}^0$ , and the latter ones refer to the lithium insertion into carbon. It is noted that the irreversible part of capacity caused by the formation of SEI and decomposition of electrolyte is also included in these potential ranges. Totally, the cathodic peaks corresponding to the reduction of  $\text{Mn}^{2+}$  to  $\text{Mn}^0$  show a shift of potential to higher values with increased amount of carbon matrix. Further, the intensity of the peaks corresponding to the reduction of  $\text{Mn}^{2+}$  to  $\text{Mn}^0$  also shows a decreasing tendency with the increasing amount of carbon. In comparison, the glycine-derived carbon electrode ng presents a single sharp cathodic peak at around 0.01 V. From the second cycle, the covered areas of all electrodes are reduced, indicating the irreversible part of capacity formed in the first cycle; further, the composite electrodes present two cathodic peaks corresponding to the reduction of  $\text{Mn}^{2+}$  to  $\text{Mn}^0$  and the lithium insertion into carbon, respectively. In the opposite anodic scans, the main peaks located at around 1.0–1.3 V can be attributed to the oxidation of  $\text{Mn}^0$  to  $\text{Mn}^{2+}$ . Totally, the anodic peaks show a shift of peak potential to lower values as the increased amount of carbon matrix. Therefore, the samples n4, n5, and n6 show smaller discharge-charge polarization than samples n2.5 and n3. The same conclusion was also confirmed in the former galvanostatic discharge-charge measurement.

To further explore the rate capability of the MnO/C composites, current rates were increased from 0.4  $\text{A g}^{-1}$  to 3.0  $\text{A g}^{-1}$  and then decreased to 0.4  $\text{A g}^{-1}$  to test the cycling performance of selected samples n4, n5, and n6, as shown in Figure 9. Decisively, sample n4 demonstrates the best rate capability. The corresponding reversible capacities at 0.4, 0.7, 1.0, 1.5, 2.0, 2.5, and 3.0  $\text{A g}^{-1}$  are approximately 583, 543, 493, 423, 367, 323, and 286  $\text{mAh g}^{-1}$ , respectively. The capacities at higher

currents fade rapidly, which is ascribed to the polarization effect at increased current rates. However, a satisfactory reversible capacity of about 553 mAh g<sup>-1</sup> can be restored after 150 cycles upon reducing the current rate to 0.4 A g<sup>-1</sup>. Sample n5 shows a similar rate performance but slightly lower capacities as compared to sample n4. Sample n6 shows the worst rate capability and the capacities are greatly decreased as the increase of current density.

In conclusion, a proper amount of carbon matrix (such as samples n4 and n5) can provide good electronic connection and alleviate the stress caused by volume change, thus improve the cycling performance and rate capability. However, overmuch carbon (such as sample n6) could decrease the overall capacity of the composite and impede the lithium migration speed, thus the electrode present lower capacities and bad rate capability. Figure 10 shows the typical SEM images at different magnifications after a cycling test of more than 100 cycles. The cubic crystals exhibit cracks after cycling. However, thanks to the carbon matrix, the cubic crystals are firmly embedded in the matrix. Therefore, the carbon matrix provides a great buffering effect to alleviate the volume change of oxides during lithium insertion/extraction. While local crack or pulverization occurs in some large oxide crystals, the carbon matrix prevents the oxide from being isolated from the electrode. In addition, the carbon matrix offers a connected structure for fast Li ion and electron transportation, beneficial to the enhanced cycling and rate performances. Moreover, the N-doping characteristic of the carbon matrix offers more Li storage sites than graphitic carbon, increasing the capacity as stored in carbon.<sup>20, 21, 27, 28</sup>

In order to compare various MnO-based anodes, Table 2 summarizes their electrochemical performance. Obviously, in comparison to previous reports,<sup>11, 20, 23, 29, 30</sup> our sample demonstrates a high specific capacity, good cycling stability, and superior rate performance, which is credited to the incorporation of MnO nanoparticles into the N-doped carbon matrix.

Table 1. Summary of the cycling performance at 0.5 A g<sup>-1</sup>

Sample	Q <sub>chl</sub> mAh g <sup>-1</sup>	Q <sub>disl</sub> mAh g <sup>-1</sup>	Initial Coulombic efficiency [%]	Q <sub>chl10</sub> mAh g <sup>-1</sup>	Retention efficiency Q <sub>chl</sub> /Q <sub>chl10</sub> [%]
n2.5	487.95	939.71	51.93	138.55	28.39
n3	511.62	788.36	64.90	322.24	62.98
n4	578.25	861.50	67.12	556.03	96.16
n5	604.11	925.48	65.28	533.81	88.36
n6	519.93	915.99	56.76	438.29	84.30
ng	308.16	764.83	40.29	204.46	66.35

Table 2. Comparison of the electrochemical performance of various MnO materials

Samples	Current density $\text{g}^{-1}$	Cycle A numbe r	Initial charge capacity $\text{mAh g}^{-1}$	Reversible capacity	Capacity retention (%)	Ref.
MnO nanoparticles-carbon composite	0.5	110	578.25	556.03	96.16	This work
MnO nanoparticles within spherical carbon matrix	0.5	300	621	501	81.00	23
MnO@C microspheres	0.1	60	768	625	81.38	11
lantern-like MnO@N-C	0.2	400	810.2	640	79.00	20
carbon-coated MnO porous microspheres	0.1	100	~640	525	82.03	29
MnO multi-core@N-doped carbon shell nanoparticles	0.1	60	~847	~578	~68.24	30

#### **4. Conclusions**

In conclusion, MnO/C composites with different contents of N-doped carbon were successfully synthesized by a facile thermal decomposition of manganese nitrate-glycine gels followed by calcination treatment. MnO nanocrystals were uniformly dispersed in the carbon matrix. The composites showed high discharge-charge capacities, superior cycling performance, and excellent rate capability. The greatly enhanced performance originates from the highly dispersed phase of MnO nanocrystals that provide the most active sites for lithium storage reaction, and the continuous phase of the N-doped carbon matrix that acts as an excellent electronic conduction network and a buffer to alleviate the volume change of MnO during cycling. The easy production and superior electrochemical properties of the composite indicate promising applications in high performance lithium ion batteries. The simple and cost-effective synthetic approach could be extended to produce other metal oxides and carbon composites for versatile applications.

#### **Acknowledgements**

This work was financially supported partially by the Japan Society for Promotion of Science (JSPS) and Marubun Research Promotion Foundation.



## References

1. J. B. Goodenough and K.-S. Park, *Journal of the American Chemical Society*, 2013, **135**, 1167-1176.
2. M. M. Thackeray, C. Wolverton and E. D. Isaacs, *Energy & Environmental Science*, 2012, **5**, 7854-7863.
3. M. V. Reddy, G. V. Subba Rao and B. V. R. Chowdari, *Chemical Reviews*, 2013, **113**, 5364-5457.
4. J. Jiang, Y. Li, J. Liu, X. Huang, C. Yuan and X. W. Lou, *Advanced Materials*, 2012, **24**, 5166-5180.
5. Y. Deng, L. Wan, Y. Xie, X. Qin and G. Chen, *RSC Advances*, 2014, **4**, 23914-23935.
6. J. Yue, X. Gu, L. Chen, N. Wang, X. Jiang, H. Xu, J. Yang and Y. Qian, *Journal of Materials Chemistry A*, 2014, **2**, 17421-17426.
7. K. Su, C. Wang, H. Nie, Y. Guan, F. Liu and J. Chen, *Journal of Materials Chemistry A*, 2014, **2**, 10000-10006.
8. L. Chang, L. Mai, X. Xu, Q. An, Y. Zhao, D. Wang and X. Feng, *RSC Advances*, 2013, **3**, 1947-1952.
9. J. Gao, M. A. Lowe and H. D. Abruña, *Chemistry of Materials*, 2011, **23**, 3223-3227.
10. X. Qin, H. Zhang, J. Wu, X. Chu, Y.-B. He, C. Han, C. Miao, S. Wang, B. Li and F. Kang, *Carbon*, 2015, **87**, 347-356.
11. X. Wang, S. Qiu, G. Lu, C. He, J. Liu, L. Luan and W. Liu, *CrystEngComm*, 2014, **16**, 1802-1809.
12. S. Luo, H. Wu, Y. Wu, K. Jiang, J. Wang and S. Fan, *Journal of Power Sources*, 2014, **249**, 463-469.
13. G. Lu, S. Qiu, H. Lv, Y. Fu, J. Liu, X. Li and Y.-J. Bai, *Electrochimica Acta*, 2014, **146**, 249-256.
14. C. Zhu, G. Saito and T. Akiyama, *Journal of Alloys and Compounds*, 2015, **646**, 639-646.
15. C. Yang, Q. Gao, W. Tian, Y. Tan, T. Zhang, K. Yang and L. Zhu, *Journal of Materials Chemistry A*, 2014, **2**, 19975-19982.
16. X. Li, Y. Zhu, X. Zhang, J. Liang and Y. Qian, *RSC Advances*, 2013, **3**, 10001-10006.
17. J. Wang, L. Shen, P. Nie, X. Yun, Y. Xu, H. Dou and X. Zhang, *Journal of Materials Chemistry A*, 2015, **3**, 2853-2860.
18. G. Wang, J. Zhang, S. Kuang, J. Zhou, W. Xing and S. Zhuo, *Electrochimica Acta*, 2015, **153**, 273-279.
19. X. Gu, J. Yue, L. Chen, S. Liu, H. Xu, J. Yang, Y. Qian and X. Zhao, *Journal of Materials Chemistry A*, 2015, **3**, 1037-1041.
20. T. Qiu, J. Wang, Y. Lu and W. Yang, *RSC Advances*, 2014, **4**, 23027-23035.
21. K. Zhang, X. Li, J. Liang, Y. Zhu, L. Hu, Q. Cheng, C. Guo, N. Lin and Y. Qian, *Electrochimica Acta*, 2015, **155**, 174-182.
22. X. Li, X. Zhu, Y. Zhu, Z. Yuan, L. Si and Y. Qian, *Carbon*, 2014, **69**, 515-524.
23. H. Hu, H. Cheng, Z. Liu and Y. Yu, *Electrochimica Acta*, 2015, **152**, 44-52.
24. X. Li, D. Li, L. Qiao, X. Wang, X. Sun, P. Wang and D. He, *Journal of Materials Chemistry*, 2012, **22**, 9189-9194.
25. Q. Qu, T. Gao, H. Zheng, X. Li, H. Liu, M. Shen, J. Shao and H. Zheng, *Carbon*, 2015, **92**, 119-125.
26. Y. Xu, J. Feng, X. Chen, K. Kierzek, W. Liu, T. Tang and E. Mijowska, *RSC Advances*, 2015, **5**, 28864-28869.

27. C. Zhu, N. Sheng and T. Akiyama, *RSC Advances*, 2015, **5**, 21066-21073.
28. C. Zhu, G. Saito and T. Akiyama, *Journal of Alloys and Compounds*, 2015, **633**, 424-429.
29. S. Guo, G. Lu, S. Qiu, J. Liu, X. Wang, C. He, H. Wei, X. Yan and Z. Guo, *Nano Energy*, 2014, **9**, 41-49.
30. H. Liu, Z. Li, Y. Liang, R. Fu and D. Wu, *Carbon*, 2015, **84**, 419-425.

Figure 1. (a) XRD patterns and (b) Raman spectra of the obtained products.

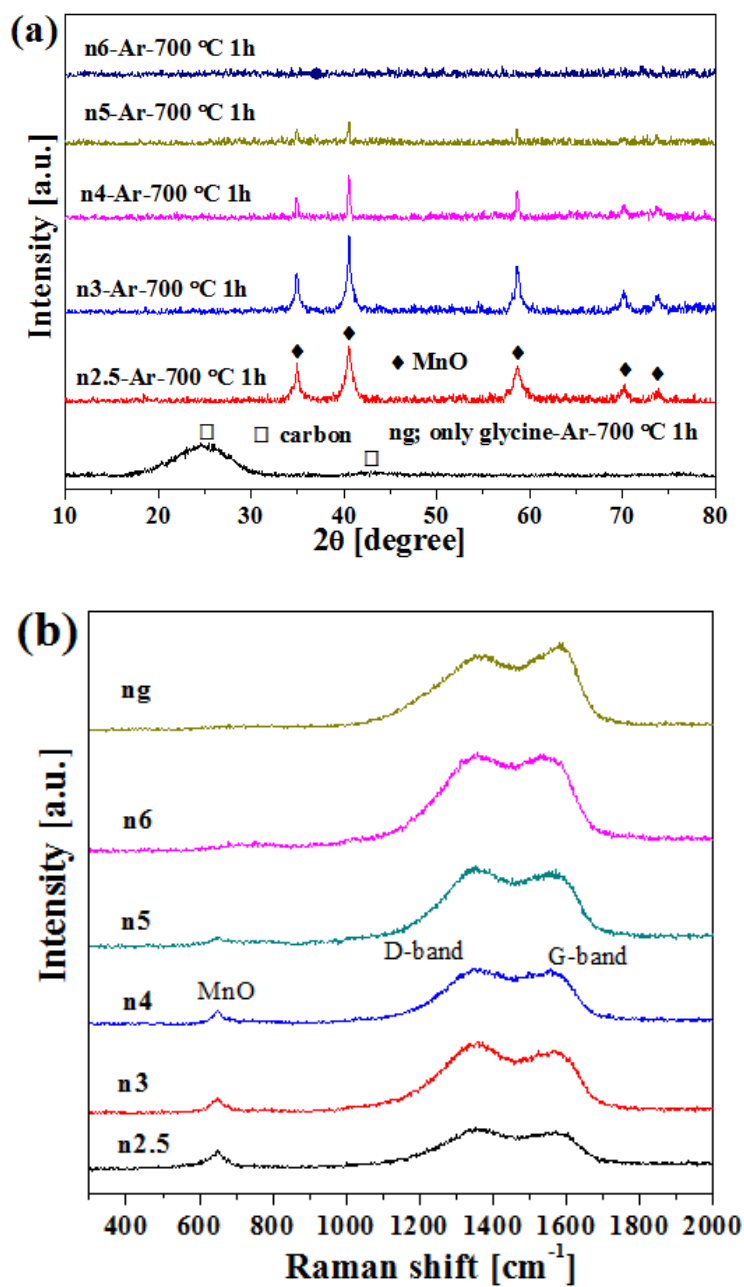


Figure 2. XPS spectra of the obtained samples: (a) survey scan, (b) N 1s spectrum, and (c) C 1s spectrum.

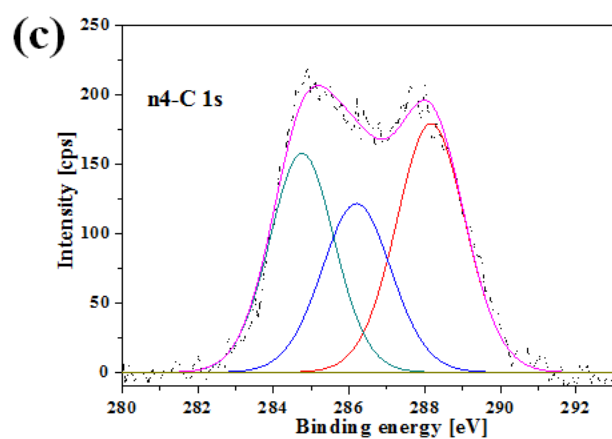
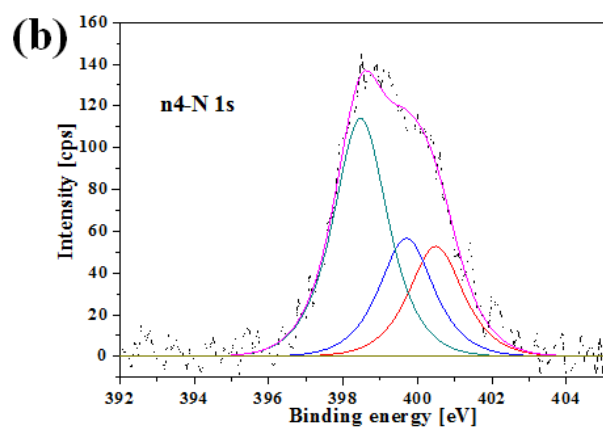
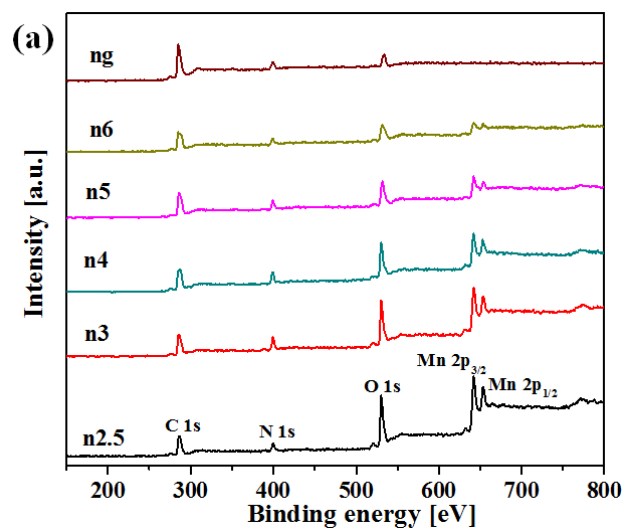


Figure 3. TG curves of the obtained samples under air flow.

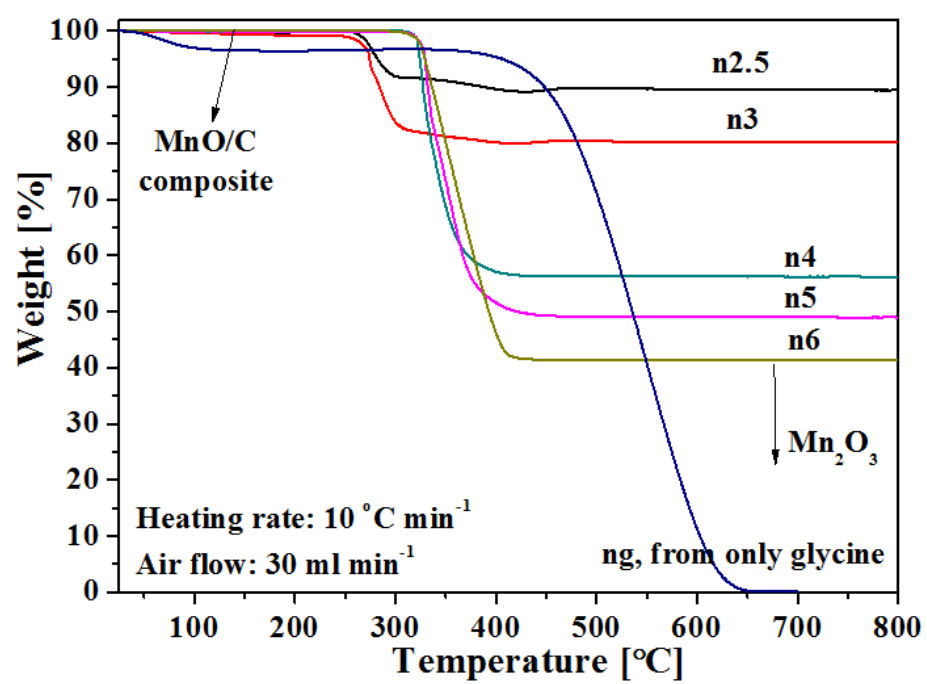


Figure 4. SEM images of the obtained products at different magnifications and the EDS mapping of sample n4 showing oxygen and manganese elements.

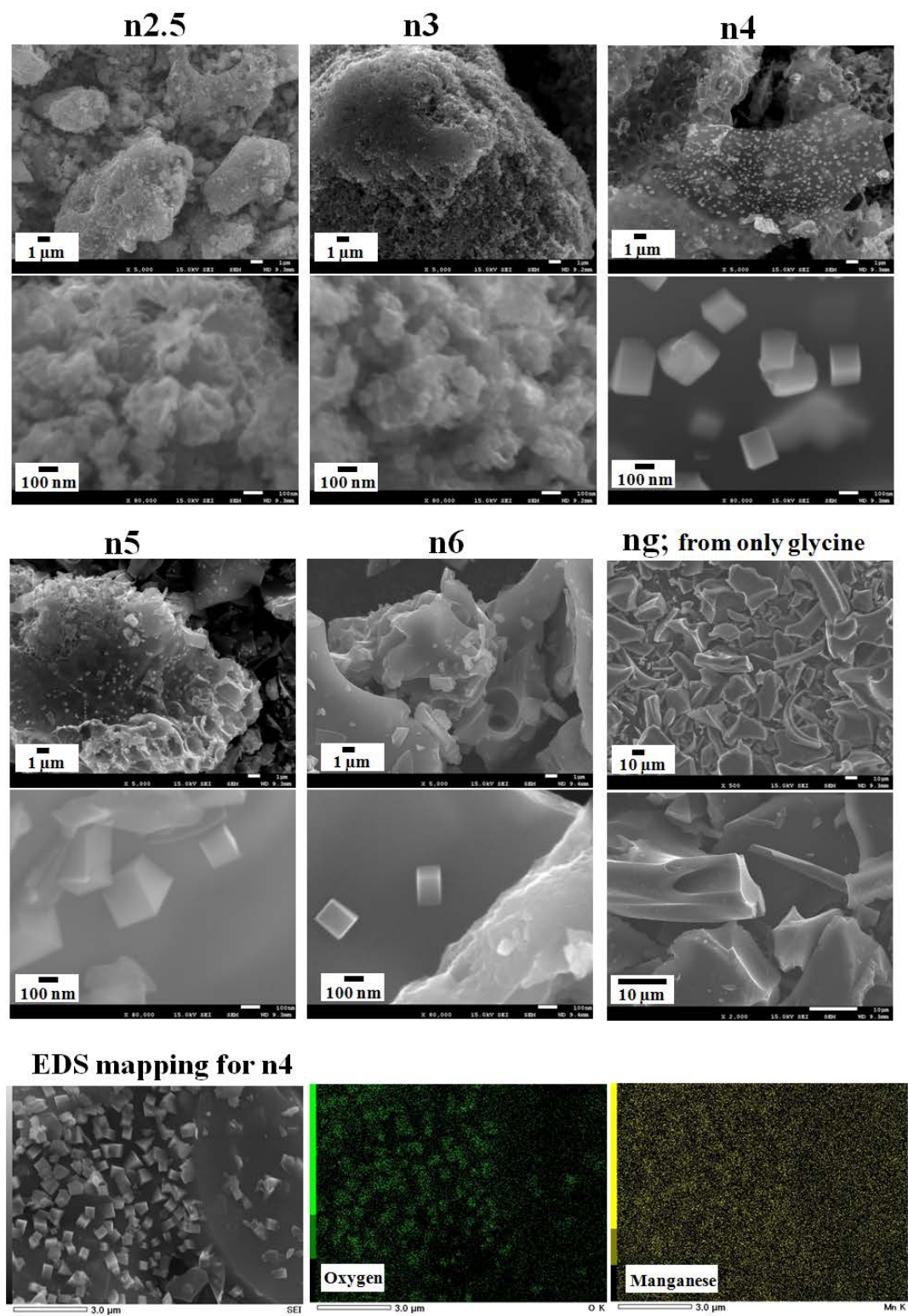


Figure 5. TEM image (a) and high-resolution TEM image (b) for sample n4. Inset shows the typical selected area diffraction pattern.

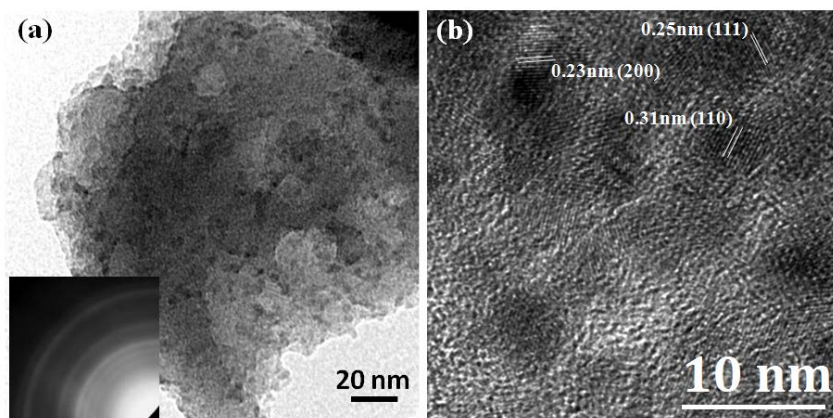


Figure 6. Cycling performance of the obtained samples. (a) Discharge/charge capacities at a current density of  $0.5 \text{ A g}^{-1}$ ; (b) the corresponding Coulombic efficiency.

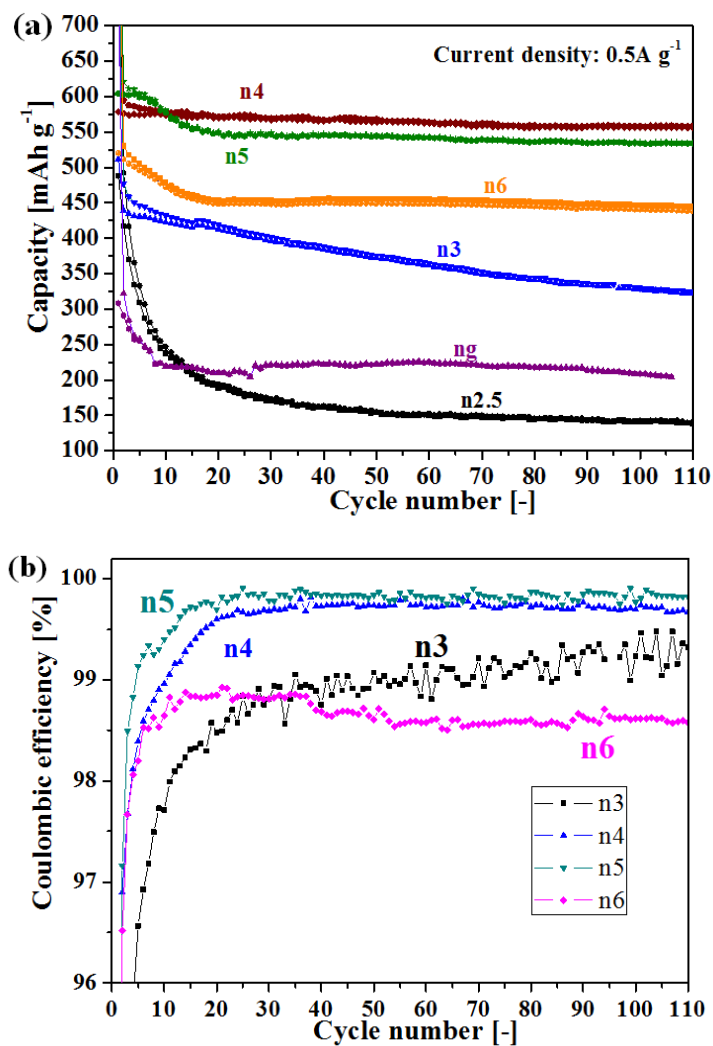


Figure 7. Discharge/charge curves of the samples at various cycles.

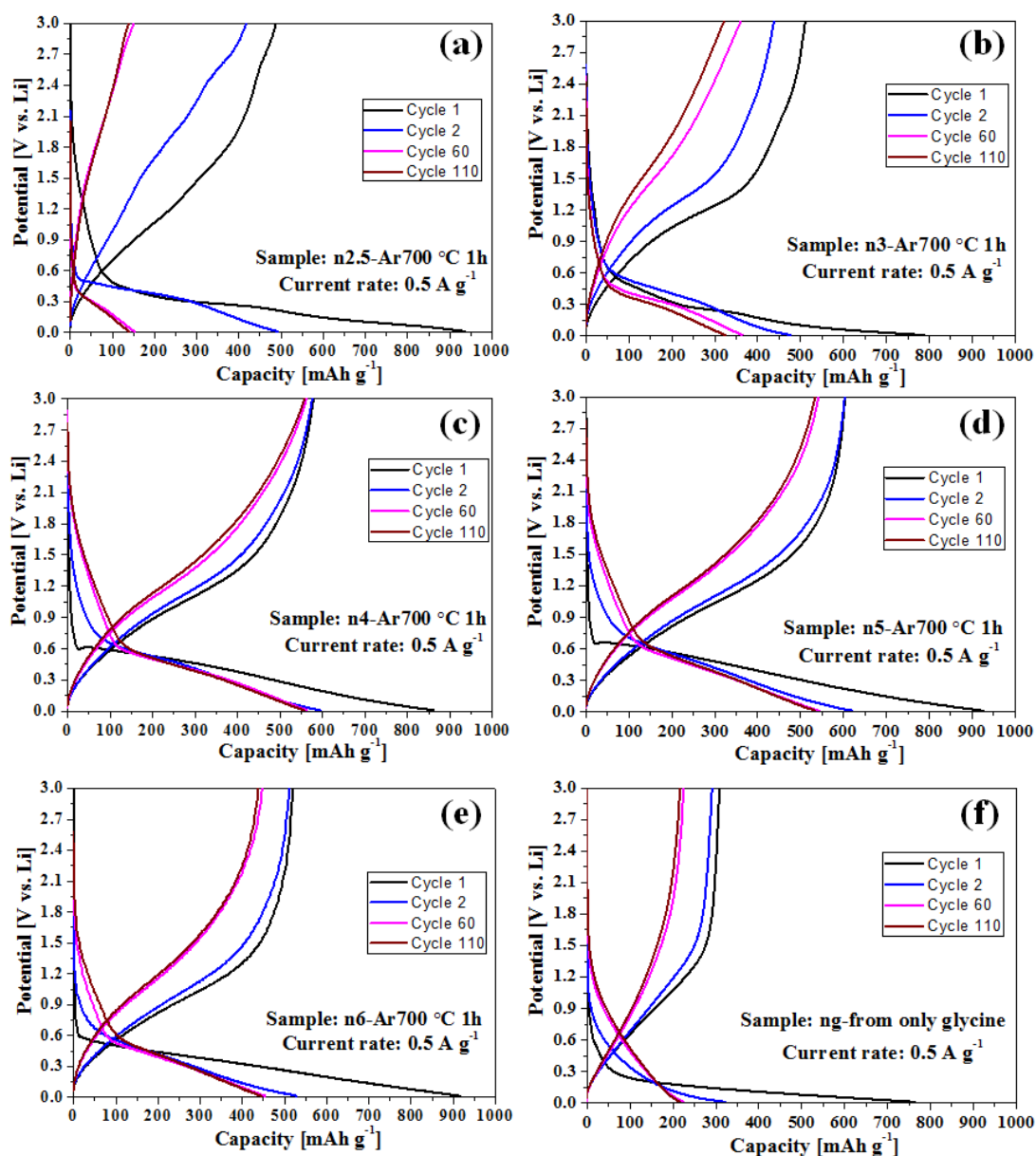




Figure 8. CV curves of the samples at a scan rate of  $0.1 \text{ mV s}^{-1}$ .

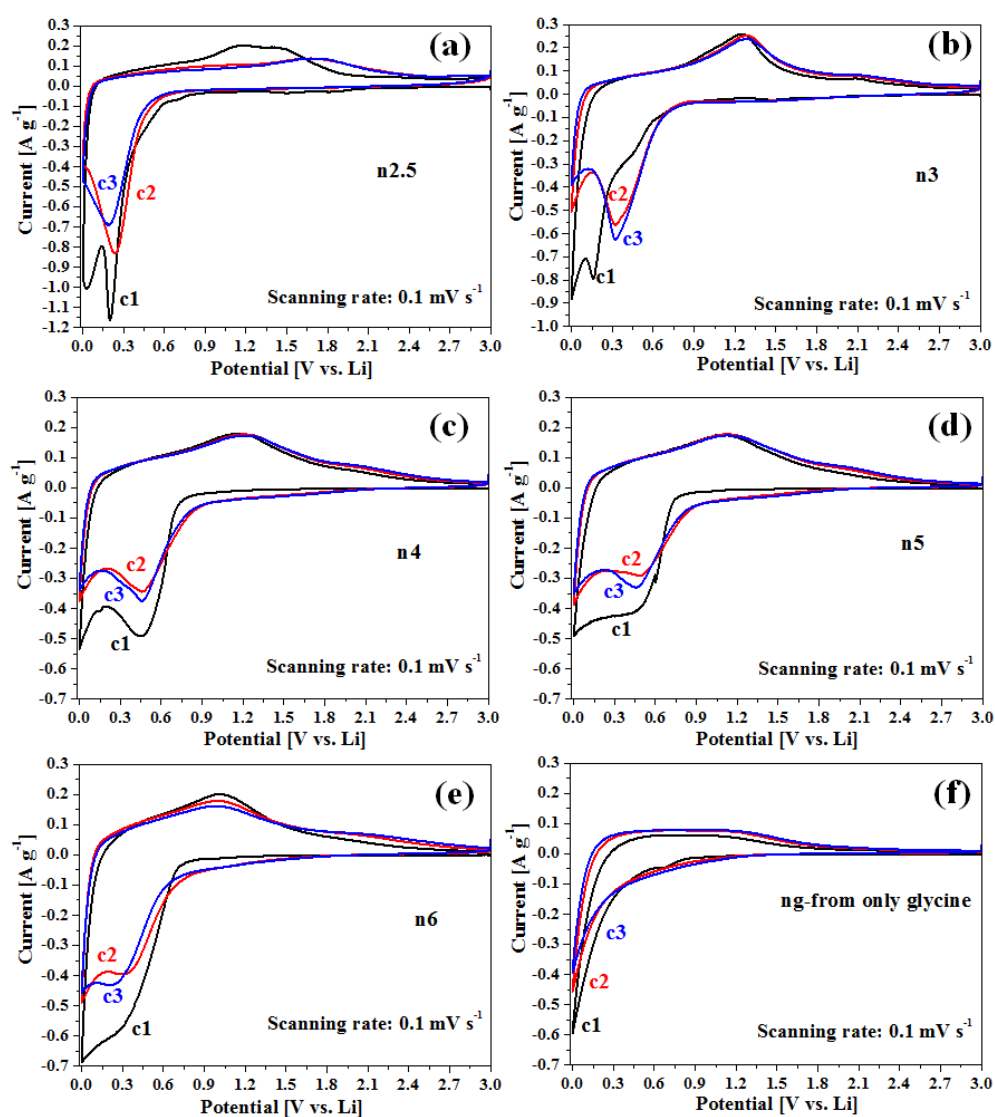


Figure 9. Cycling performance of the samples at varying current rates.

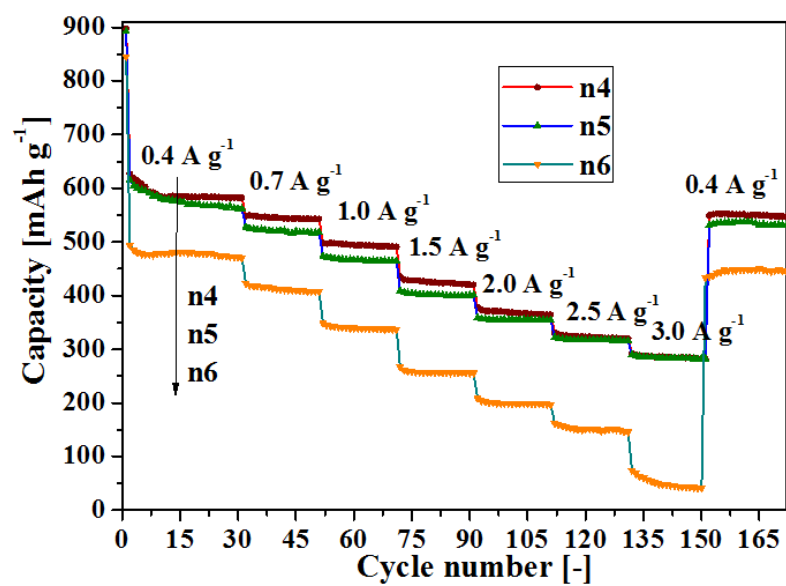


Figure 10. SEM images at different magnifications of sample n4 after 110 cycles of discharge and charge.

